Check for updates

small methods
www.small-methods.com

A Microfluidic System for Simultaneous Raman Spectroscopy, Patch-Clamp Electrophysiology, and Live-Cell Imaging to Study Key Cellular Events of Single Living Cells in Response to Acute Hypoxia

Fenja Knoepp, Joel Wahl, Anders Andersson, Simone Kraut, Natascha Sommer, Norbert Weissmann,* and Kerstin Ramser**

The ability to sense changes in oxygen availability is fundamentally important for the survival of all aerobic organisms. However, cellular oxygen sensing mechanisms and pathologies remain incompletely understood and studies of acute oxygen sensing, in particular, have produced inconsistent results. Current methods cannot simultaneously measure the key cellular events in acute hypoxia (i.e., changes in redox state, electrophysiological properties, and mechanical responses) at controlled partial pressures of oxygen (pO_2). The lack of such a comprehensive method essentially contributes to the discrepancies in the field. A sealed microfluidic system that combines i) Raman spectroscopy, ii) patch-clamp electrophysiology, and iii) live-cell imaging under precisely controlled pO_2 have therefore been developed. Merging these modalities allows label-free and simultaneous observation of oxygen-dependent alterations in multiple cellular redox couples, membrane potential, and cellular contraction. This technique is adaptable to any cell type and allows in-depth insight into acute oxygen sensing processes underlying various physiologic and pathologic conditions.

1. Introduction

Hypoxia (i.e., oxygen (O_2) shortage in tissues and cells) is not only crucially involved in physiological conditions, such as angiogenesis[1] or erythropoiesis[2] but also critically contributes to the pathogenesis of major global causes of mortality, such as myocardial ischemia, stroke, chronic lung disease, and cancer.[3–6]

To minimize fatalities and pathological consequences of acute or chronic O_2 deficiency, the ability to sense and adapt to hypoxia is of fundamental importance.[7] Consequently, understanding the molecular processes and pathways underlying O_2 sensing may aid the development of new treatment strategies for human diseases that are related to O_2 deficiency. However, despite major advances in understanding the cellular response to chronic hypoxia via hypoxia-inducible factor (HIF) signaling, the mechanisms modulating this pathway (e.g., via mitochondrial metabolites or reactive oxygen species (ROS)) remain controversial.[8] Moreover, despite intense research over the last decades, the underlying molecular mechanism of acute cellular O_2 sensing, in particular, the acute response to mild hypoxia is not yet fully elucidated and severe controversies exist.[8,9] There is, however, a consensus that conserved features of acute O_2 sensing in mammalian cells include i) an alteration in the redox state that is determined by mitochondria or reduced nicotinamide adenine dinucleotide phosphate (NADPH) oxidases and ii) a change in activity of O_2-sensitive ion channels such as voltage-gated potassium (K^+) channels, controlling membrane potential. Such sensing processes trigger cell-type specific responses to hypoxia, for example, the contraction or relaxation of vascular smooth muscle cells.[7,10,11] Furthermore, they may induce prolonged responses affecting chronic O_2 sensing, such as HIF modulation by succinate accumulation or changes in ROS.[12] Although these processes are pivotal for maintaining O_2 homeostasis (e.g., carotid-body-mediated adaptation of respiratory frequency and heart rate or modulation of the vascular tone by O_2 demand), the exact contributions of the different

F. Knoepp, S. Kraut, N. Sommer, N. Weissmann
Excellence Cluster Cardio-Pulmonary Institute (CPI)
University of Giessen and Marburg Lung Center (UGMLC)
Member of the German Center for Lung Research (DZL)
Justus-Liebig-University, Giessen
D-35392 Giessen, Germany
E-mail: fenja.knoepp@innere.med.uni-giessen.de;
norbert.weissmann@innere.med.uni-giessen.de
J. Wahl, A. Andersson, K. Ramser
Department of Engineering Sciences and Mathematics
Luleå University of Technology
Luleå SE-97187, Sweden
E-mail: kerstin.ramser@ltu.se

The ORCID identification number(s) for the author(s) of this article can be found under https://doi.org/10.1002/smtd.202100470.

© 2021 The Authors. Small Methods published by Wiley-VCH GmbH. This is an open access article under the terms of the Creative Commons Attribution-NonCommercial-NoDerivs License, which permits use and distribution in any medium, provided the original work is properly cited, the use is non-commercial and no modifications or adaptations are made.

DOI: 10.1002/smtd.202100470

23669608, 2021, 10, Downloaded from https://onlinelibrary.wiley.com/doi/10.1002/smtd.202100470 by Justus-Liebig-Universitat, Wiley Online Library on [24/11/2022]. See the Terms and Conditions (https://onlinelibrary.wiley.com/terms-and-conditions) on Wiley Online Library for rules of use; OA articles are governed by the applicable Creative Commons License

mitochondrial complexes, NADPH oxidases, and cellular redox state to O_2 sensing remain unclear.

To date, one of the major limitations (and at least partly the cause of the discrepancies) in studies of the multifactorial processes underlying cellular O_2 sensing has been the requirement for the use of several complementary techniques. A comprehensive technology allowing simultaneous assessment of the cellular and mitochondrial redox state, membrane potential, and cellular functional reactivity along with tight control over partial O_2 pressure (pO_2) has not been available. Furthermore, the methods often used to assess the cellular redox state (imaging techniques based on fluorescent dyes,[13] for example, NAD(P)H autofluorescence,[14] overexpressed fluorescent redox-sensitive proteins,[15] NAD(P)H-specific sensors,[16] or spectrophotometry,[17] or biochemical techniques such as liquid chromatography or immunoblotting)[18–21] have important limitations. The biochemical techniques require staining, fixation, and destruction of cells or tissues, and consequently only allow investigation of a certain biomarker at a single timepoint. The imaging techniques can be combined with other techniques and are generally valuable for tempo spatial analysis of the redox state, but they can only investigate a few biomolecules simultaneously. Furthermore, imaging techniques pose a potential risk for cross-reactions of overexpressed proteins or fluorescent dyes with other cellular redox couples.[22]

Use of Raman spectroscopy to assess the mitochondrial and cellular redox state avoids the limitations associated with biochemical and imaging techniques. Raman spectroscopy can detect a range of biomarkers (e.g., DNA, lipids, and proteins) in a single spectrum without staining or destruction of the sample,[23,24] and is currently one of the most precise options to measure the cellular and mitochondrial redox state in living cells. In addition, Raman spectroscopy can be combined with patch-clamp electrophysiology,[25,26] which enables high-resolution recordings of membrane potential and ionic currents—even on single-channel level—in excised membrane patches, individual cells, or tissue sections.[27] Due to its unrivaled signal-to-noise ratio, patch-clamp electrophysiology is regarded as the gold standard for the measurement of cellular electrophysiological responses to hypoxia.[3,4,8,9] However, studying the electrophysiological response to acute hypoxia requires precise regulation of pO_2 and rapid switching between normoxia and hypoxia, while still allowing access for the patch pipette. Application of acute hypoxia in open patch-clamp chambers by continuous perfusion with solutions purged with hypoxic gas mixtures[8,26,28] often leads to reoxygenation due to dilution with ambient O_2, rendering tight control over pO_2 impossible and delaying the application of acute hypoxia to the cells.[26] The need for precise regulation of pO_2 resulted in the development of a microfluidic system with a fixed patch-clamp pipette and optical tweezers to steer single suspended cells towards the pipette.[29] However, no full patch-clamp protocol could be established and the measurement of adherent cells, such as pulmonary arterial smooth muscle cells (PASMCs), was inoperable. More recently, we developed a sealed microfluidic system that allowed simultaneous Raman spectroscopy and the general possibility to perform patch-clamp electrophysiology via a mobile patch-clamp pipette.[26]

We have now further improved our approach, constructing an innovative microfluidic system that combines Raman spectroscopy and patch-clamp electrophysiology—the current gold standards for the investigation of the cellular redox state and electrophysiological properties—with simultaneous live-cell imaging to determine the contraction of single living PASMCs that are acutely exposed to precisely defined levels of pO_2. PASMCs are specialized oxygen sensing cells that contract in response to acute hypoxia which helps the pulmonary vasculature to divert blood from poorly oxygenated to well-oxygenated lung areas and thereby optimize arterial pO_2. The technique presented here can be easily adapted to any other cell type and adjusted to other biomarkers of interest, and thereby provides for the first time the unique opportunity to measure directly and simultaneously the key features of O_2 sensing (i.e., biomolecular, electrophysiological, and mechanical responses) in single living cells.

2. Results

2.1. Design and Manufacturing of the Microfluidic System

The design of the microfluidic system was based on i) the number of required in- and outlet pipes (i.e., inflow, outflow, patch pipette, reference electrode, and O_2 sensor) and ii) the shape of the culture dishes used for cell culture (**Figure 1**a–d). The lower opening of the pipe for the patch pipette (= measurement section) was centered in the microfluidic system (see Figure 1c and Figure S1, Supporting Information). Consequently, a cell within the boundaries of the measurement section was accessible to the patch pipette for electrophysiological recordings while being at the same time centered to the beam pass for laser and LED light for Raman spectroscopy and live-cell imaging, respectively. When assembled with the cell culture dish, the microfluidic channel's height was determined by the distance between the underpart of the microfluidic system and the dish's lowered glass bottom, which was 175 µm.

Microfluidic systems are extremely sensitive to changes in pressure or flow rates. Such alterations might cause the fluid to rise into the pipes of the microfluidic system, which would not only hamper patch-clamp recordings but also delay the transition between oxygenation states due to the unintended mixing of distinct perfusates. To determine the fluid level and velocity in the measurement section for different pipe-diameters, we performed time-dependent simulations using computational fluid dynamics.[30] A volume of fluids model was implemented to account for both the gas and liquid phase (for more details see the Methods section). The results of this simulation are summarized in **Table 1** and show the predicted fluid build-up in the measurement section for different diameters of the inlet, outlet, and patch pipette channel. The simulations confirmed a well-ordered flow inside the microfluidic system (Figure 1e) and no significant rise of fluid into the pipes could be detected (Figure 1f and Table 1) when an inlet diameter of 2.0 mm, outlet of 5.0 mm, and patch pipette channel of 7.0 mm was chosen. Detailed technical specifications on the final pipe's dimensions, that is, diameters and angles, are provided in **Table 2** and Figure S1, Supporting Information, respectively.

Upon design, the microfluidic system was manufactured from a monolithic piece of polymethylpentene, a polymer showing little interference with the Raman lines of the

© 2021 The Authors. Small Methods published by Wiley-VCH GmbH

23669608, 2021, 10, Downloaded from https://onlinelibrary.wiley.com/doi/10.1002/smtd.202100470 by Justus-Liebig-Universitat, Wiley Online Library on [24/11/2022]. See the Terms and Conditions (https://onlinelibrary.wiley.com/terms-and-conditions) on Wiley Online Library for rules of use; OA articles are governed by the applicable Creative Commons License

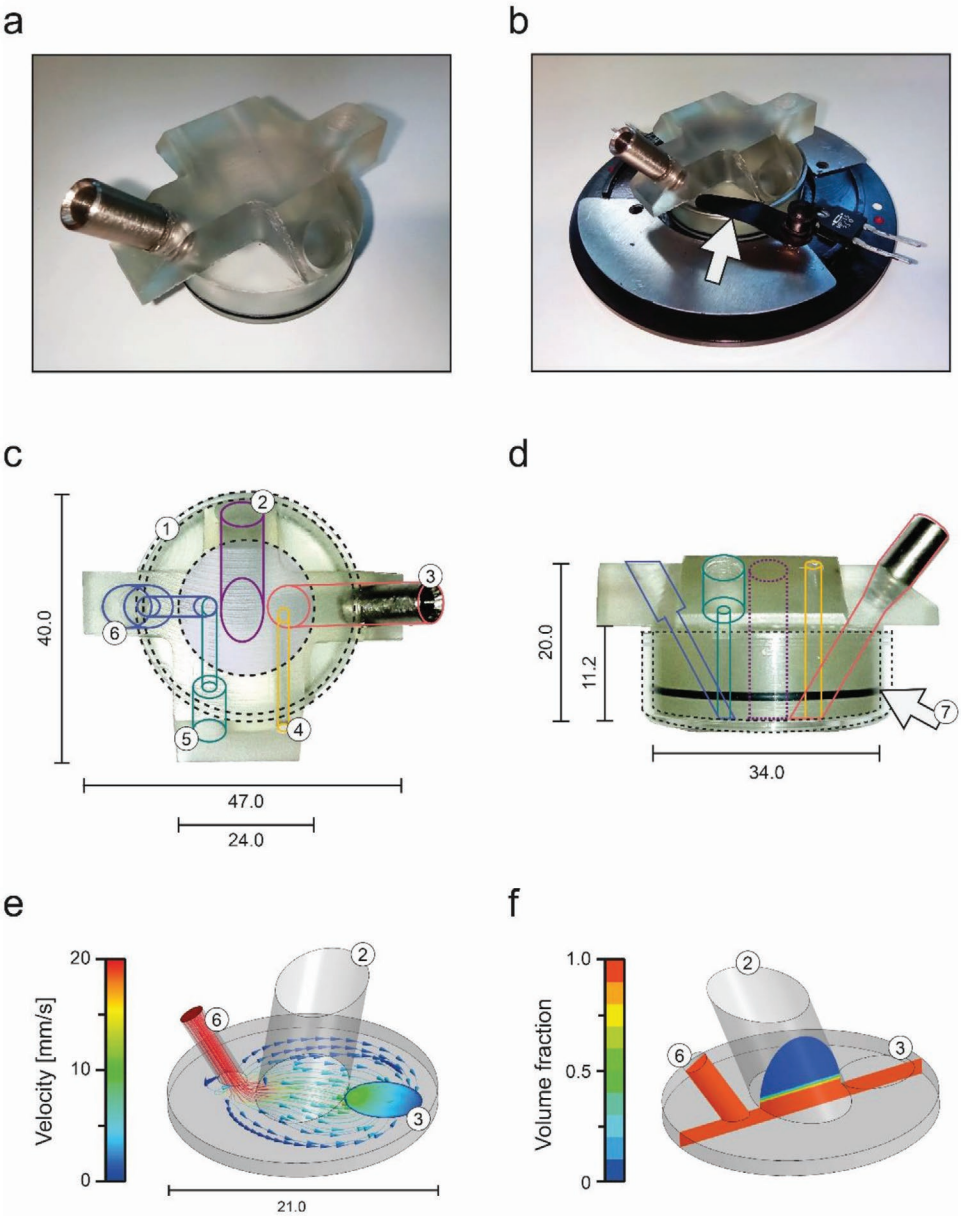

Figure 1. Design of the sealed microfluidic system. a) Isometric photograph of the microfluidic system. b) To prevent unwanted movements during experiments, the microfluidic system was securely fixed to the microscope stage via clamps (highlighted with a white arrow). c) Top and d) side view of the microfluidic system (①), containing pipes for the patch pipette (②), outlet (③), reference electrode (④), O_2 sensor (⑤), inlet (⑥), and sealing ring (⑦). Dimensions are given in mm. e) Streamlines of velocity of the liquid phase from inlet to outlet. Arrows display the fluid velocity sampled with 1 s rate. f) The volume fraction of the liquid phase in a vertical plane at $t = 100$ s indicates a negligible fluid build-up in the pipe for the patch pipette.

targeted biomarkers cytochrome c (with reduced/oxidized iron (Fe^{2+}/Fe^{3+})), as well as the reduced and oxidized form of nicotinamide adenine dinucleotide (NADH and NAD^+, respectively). (Figure S2, Supporting Information). The pipes of the distinct components were milled by computed numerical control (CNC) drilling (see Table 2 and Figure S1, Supporting Information, for technical specifications). To ensure easy handling and insertion into the culture dish as well as the possibility to fix the system to the microscope stage, excess material was removed from the microfluidic system (see Figure 1a,b and Figure S1, Supporting Information).

2.2. Sample Preparation and Experimental Procedure

Murine PASMCs from C57BL/6J mice were isolated 7 to 10 days prior to experiments and grown on commercially available glass bottom dishes that were subsequently used for the experiments.

In preparation for the experiments, the reference electrode, O_2 sensor, and inlet and outlet tubes were mounted to their respective pipes within the microfluidic system. To avoid any air or fluid leakage, these components were either tightly fit to their respective channels or sealed via polyetheretherketone

© 2021 The Authors. Small Methods published by Wiley-VCH GmbH

23669608, 2021, 10, Downloaded from https://onlinelibrary.wiley.com/doi/10.1002/smtd.202100470 by Justus-Liebig-Universitat, Wiley Online Library on [24/11/2022]. See the Terms and Conditions (https://onlinelibrary.wiley.com/terms-and-conditions) on Wiley Online Library for rules of use; OA articles are governed by the applicable Creative Commons License

Table 1. Time-resolved fluid build-up in the measurements section of the microfluidic system determined by fluid simulation for distinct pipe diameters. The parameters highlighted in grey, showing the least fluid build-up, were used for manufacturing the microfluidic system.

		Fluid build-up [mm]		
Ø [mm]	Inlet	2.0	2.0	2.0
	Outlet	5.0	4.0	2.0
	Patch pipette	7.0	4.0	4.0
Time [s]	50	0.39571	1.26691	1.41328
	100	0.48592	1.26862	1.41453
	150	0.55461	1.27099	1.41624
	200	0.60666	1.27378	1.41781

(PEEK) one-piece fingertight fittings and their corresponding ferrules (see methods section for details). All components remained attached throughout the measurement day, providing simple and efficient handling. All components could be removed for cleaning purposes.

Prior to experiments, the outer edges of the microfluidic system were coated with a thin but continuous layer of vacuum grease. Although vacuum grease was found to be sufficient to prevent any lateral leakage during experiments, a sealing ring as a precautionary measure was permanently mounted to the outside of the microfluidic system (see Figure 1d).

The cell culture medium was removed from the PASMCs in the culture dish by pipetting. As the remaining fluid, that is, cell culture medium, would have hampered adequate sealing by vacuum grease, the periphery of the dish was thoroughly dried with cotton buds. Afterwards, the assembled microfluidic system was placed in the culture dish containing the PASMCs and securely fixed to the microscope stage with commercially available clamps (Warner Instruments, Hamden, USA, see Figure 1b). This tight fixation not only prohibited accidental movements of the microfluidic system during experiments but additionally provided good thermal contact to the heated microscope stage, which offered the opportunity to perform measurements at physiological temperatures, that is, 37 °C.

Upon fixation, the chamber was immediately perfused with Tyrode's solution from a gravity-driven perfusion system. This perfusion system consists of fluid reservoirs that were filled with Tyrode´s solution and gassed with either a normoxic (21% O_2, 5.3% carbon dioxide (CO_2), rest nitrogen (N_2)) or a hypoxic (1% O_2, 5.3% CO_2, rest N_2) gas mixture. The solution was delivered to the microfluidic system via a multichannel inline heater that not only preheated the solutions to 37 °C, but also served as a manifold with minimal dead space. Electronic valve control of the tubes connecting the reservoirs with the heater—and thus the microfluidic system—allowed seamless shifts between normoxic and hypoxic solutions at constant physiological temperatures.

Table 2. Specifications of diameter and angles of the different pipes.

N_O	Channel	Ø [mm]	Angle [∡]
2	Patch pipette	7.0	45°
3	Outlet	5.0	55°
4	Reference electrode	2.0	45°
5	Oxygen sensor	1.0	45°
6	Inlet	2.0	60°

Raman spectroscopy and live-cell imaging could be achieved without interference by using well-separated wavelengths (i.e., a 635 nm red light-emitting diode (LED) for imaging and a 532 nm laser (green) for Raman scattering; **Figure 2**a,b). The patch pipette was inserted and sealed with a thin-walled highly flexible rubber insulation (Figure 2b). A schematic overview of the experimental procedure is shown in Figure 2c. To summarize, measurements were performed while changing the solution from normoxia to hypoxia and back to normoxia (recovery). The pO_2 and the cellular membrane potential were continuously recorded, while images were taken during the transitions (i.e., normoxia/hypoxia and hypoxia/recovery). Raman spectra were taken when a stable membrane potential was achieved.

2.3. Raman Spectroscopy for Monitoring Redox States of Mitochondrial and Cellular Biomarkers

In respiring mitochondria, the redox state of the individual mitochondrial chain complexes is highly dynamic, depending on the O_2 supply.[31] Sufficient hypoxia can reduce individual mitochondrial chain components and result in increased cellular NADH/NAD^+ and cytochrome c Fe^{2+}/Fe^{3+} ratios, which can be estimated by Raman spectroscopy without affecting cellular integrity.[8,32,33] In order to investigate a hypoxia-mediated alteration in cellular and mitochondrial redox state in PASMCs, Raman spectra were taken under the three different conditions (normoxia, hypoxia, and recovery; Figure 2c) and processed according to the scheme shown in **Figure 3**a. For more details regarding processing and analysis of Raman data, see the Experimental Section.

The unprocessed Raman spectra featured variations between individual experiments and a background signal (Figure S3, Supporting Information). Via subtraction of the individual spectra from each experiment (hypoxia − normoxia and recovery − hypoxia), a difference spectrum was computed for each reading in order to i) eliminate spectral components that were unaffected by changes in pO_2, ii) remove the background, and iii) reduce differences between individual measurements. The resulting difference spectra for each redox state are displayed in Figure 3b.

The redox state of the targeted mitochondrial biomarkers NADH, NAD^+, and cytochrome c (Fe^{2+}/Fe^{3+}) was estimated by comparing the experimental data with reference spectra from the literature.[34,35] A linear combination indicating the difference between the experimental data and the processed reference spectra were derived through least-squares fitting. This approach allows the selective targeting of all spectral components that are connected to biomarkers of interest by studying the overall structure of the molecular vibrations. The constructed difference spectrum was finally estimated as:

$$S_{\text{Hypoxia}} - S_{\text{Normoxia}} \approx 0.12S_{\text{NADH}} - 0.29S_{\text{NAD+}} + 0.93S_{\text{cyt c(Fe}^{2+})} - 0.74S_{\text{cyt c(Fe}^{3+})} \quad (1)$$

© 2021 The Authors. Small Methods published by Wiley-VCH GmbH

23669608, 2021, 10, Downloaded from https://onlinelibrary.wiley.com/doi/10.1002/smtd.202100470 by Justus-Liebig-Universitat, Wiley Online Library on [24/11/2022]. See the Terms and Conditions (https://onlinelibrary.wiley.com/terms-and-conditions) on Wiley Online Library for rules of use; OA articles are governed by the applicable Creative Commons License

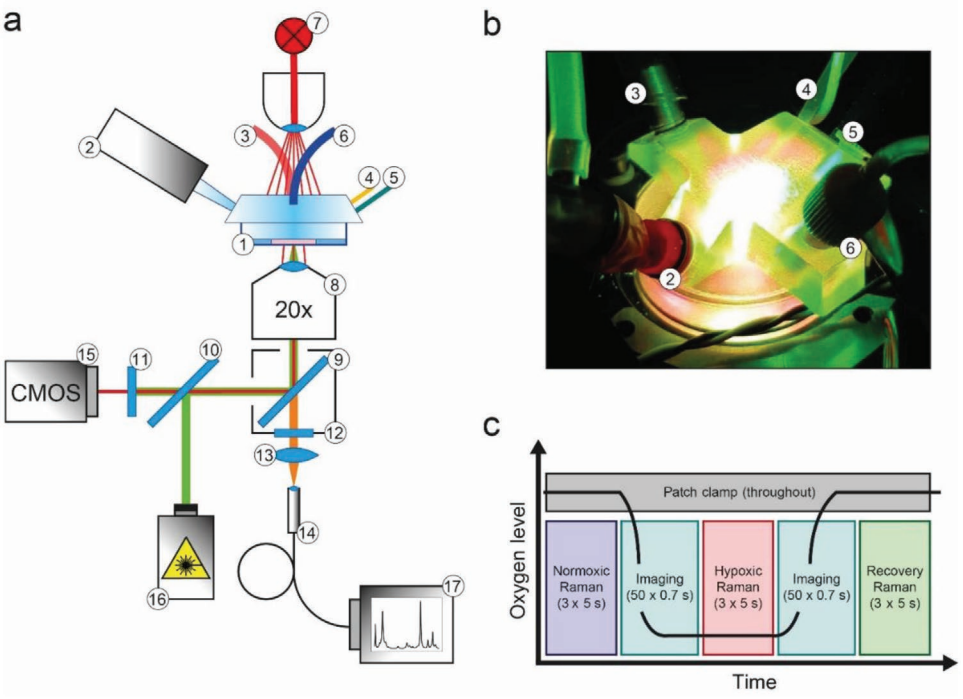

Figure 2. Experimental setup and procedure. a) Schematic depiction of the experimental setup with ① microfluidic system (in-house design), ② patch pipette (EPC 10 USB Headstage, HEKA Electronics), ③ outlet, ④ agar bridge reference electrode (ABR-1, Warner Instruments), ⑤ O_2 sensor (Bare Fiber Minisensor OXB430, Firesting O_2, PyroScience), ⑥ inlet, ⑦ light source (LED635, Thorlabs), ⑧ microscope objective (UPlanSApo, 20x, Olympus), ⑨ dichroic mirror (ZT532/640/NIRrpc, Semrock), ⑩ beamsplitter (45:55 (R:T) Pellicle, Thorlabs), ⑪,⑫ edge filter (532 EdgeBasic, Semrock), ⑬ focusing lens (Focusing Lens, 30 mm, Biconvex), ⑭ optical fiber (PN:SR-OPT-8002, LEONI Fiber Optics), ⑮ digital camera (Mako U-503B, Allied Vision), ⑯ Raman laser (532 nm, Altechna), and ⑰ Raman spectrometer (Shamrock 303i, Andor Technology). CMOS, Complementary Metal Oxide Semiconductor. b) Picture of the microfluidic system, illuminated with red LED for imaging and green laser light for Raman scattering. c) Schematic overview of the experimental procedure.

$$S_{\text{Recovery}} - S_{\text{Hypoxia}} \approx -0.38\, S_{\text{NADH}} + 0.41\, S_{\text{NAD+}} - 0.75\, S_{\text{cytc(Fe}^{2+})} + 0.63\, S_{\text{cytc(Fe}^{3+})} \quad (2)$$

where S is the spectral signal for each oxygenation state or the respective biomarker. The Raman spectra revealed that hypoxia induced an increase in NADH and cytochrome c (Fe^{2+}) while a decrease in NAD^+ and cytochrome c (Fe^{3+}) was observed (Figure 3b and **Table 3**). The opposite behavior was detected when the PASMCs were reoxygenated (recovery). The obtained linear combination was correlated with the calculated difference spectrum by 46% (Pearson's linear correlation coefficient, two-tailed: $P < 10^{-30}$) for the transition to hypoxia and by 49% (Pearson's linear correlation coefficient, two-tailed: $P < 10^{-30}$) for recovery.

The increases or decreases of each individual Raman peak of the biomarkers are presented together with the results of a one-sample t-test in Table 3.

2.4. Oxygen Sensing and Patch-Clamp Electrophysiology

Polymethylpentene is regarded as a gas-permeable polymer. To control the efficient sealing of the microfluidic system against putative and unwanted influx of environmental O_2, pO_2 was continuously recorded via an optical O_2 sensor that was placed inside the microfluidic system (Figure 1c,d). Stable hypoxic conditions of 44.9 ± 2.3 mmHg pO_2 were achieved 54.6 ± 3.0 s (mean ± SEM, n = 4) after starting perfusion of the hypoxic bath solution (**Figure 4**a). This is significantly faster than in an open perfusion system (see Figure S4, Supporting Information) which took 178.8 ± 20.0 s (mean ± SEM; n = 5; unpaired t-test, two-tailed: P = 0.0009) to achieve hypoxic conditions of a similar level, despite having an identical perfusion velocity of 1.5 mL min^{-1}. In addition, no reoxygenation-related fluctuations in pO_2—as often observed in open systems[26] or in response to undesired O_2 leakage—were detected in our improved microfluidic system (Figure 4a).

Concomitant with the evenly decreasing pO_2 (Figure 4a,b), an immediate increase in the cellular membrane potential with depolarization by 10.8 ± 4.0 mV (mean ± SEM, n = 4) was observed in patch-clamp recordings (Figure 4a,c). Interestingly, the membrane potential plateaued at a pO_2 of 44.9 ± 2.3 mmHg (mean ± SEM, n = 4), with further lowering of pO_2 showing no additional effect (Figure 4a). The extent of hypoxia-induced depolarization was similar to that observed in a conventional open system, which showed a hypoxia-induced increase in membrane potential by 11.7 ± 3.0 mV (mean ± SEM; n = 5; unpaired t-test, two-tailed: P = 0.9). However, an almost four-fold faster time course was observed in the microfluidic system: Whereas the depolarization did not plateau until 181.6 ± 18.0 s (n = 5) after initiating hypoxic exposure in an open system, a

© 2021 The Authors. Small Methods published by Wiley-VCH GmbH

23669608, 2021, 10, Downloaded from https://onlinelibrary.wiley.com/doi/10.1002/smtd.202100470 by Justus-Liebig-Universitat, Wiley Online Library on [24/11/2022]. See the Terms and Conditions (https://onlinelibrary.wiley.com/terms-and-conditions) on Wiley Online Library for rules of use; OA articles are governed by the applicable Creative Commons License

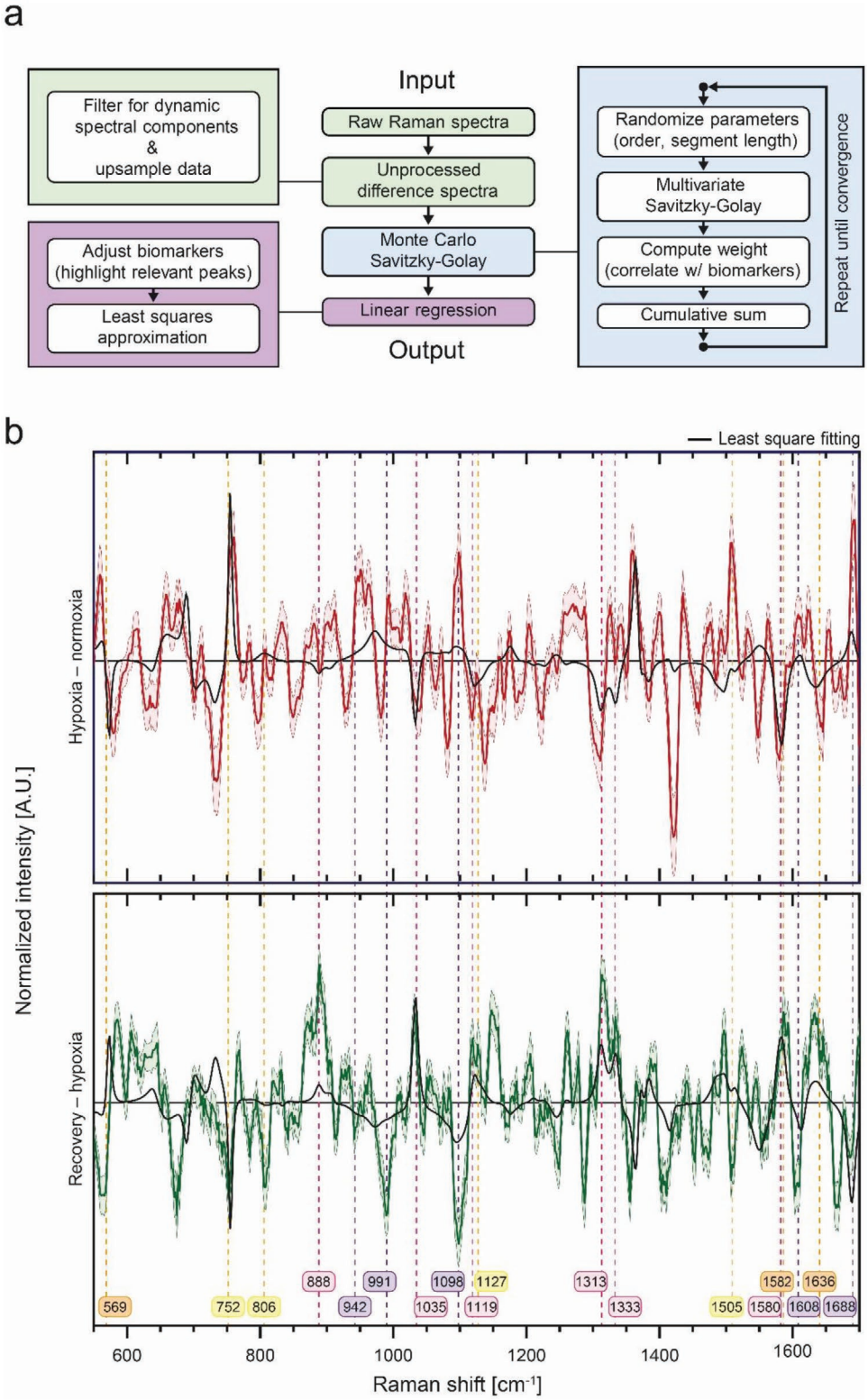

Figure 3. Raman difference spectra of PASMCs under distinct pO_2. a) Data processing scheme from raw Raman spectra to linear regression. b) Raman difference spectra of mitochondrial and cellular biomarkers in PASMCs under distinct pO_2 (hypoxia – normoxia (upper panel, red) and recovery – hypoxia (lower panel, green)). The shaded area around each trace defines the standard error of the mean (SEM), while least square fitting is shown as a black line. Dashed colored lines indicate the Raman peaks for the targeted biomarkers NADH (purple), NAD^+ (pink), and cytochrome c (Fe^{2+}, yellow; Fe^{3+}, orange). A.U., arbitrary units.

© 2021 The Authors. Small Methods published by Wiley-VCH GmbH

23669608, 2021, 10, Downloaded from https://onlinelibrary.wiley.com/doi/10.1002/smtd.202100470 by Justus-Liebig-Universitat, Wiley Online Library on [24/11/2022]. See the Terms and Conditions (https://onlinelibrary.wiley.com/terms-and-conditions) on Wiley Online Library for rules of use; OA articles are governed by the applicable Creative Commons License

Table 3. Changes in Raman peaks of mitochondrial and cellular biomarkers during transition from normoxia to hypoxia and subsequent recovery.

Biomarker	Raman peak [cm^{-1}]	Hypoxia [↑/↓]		Recovery [↑/↓]		Assignment	Reference
NADH	942	↑	($P = 0.0010$)	–	($P = 0.1000$)	Nicotinamide	[35]
	991	↑	($P = 0.0200$)	↓	($P < 0.0001$)	Nicotinamide	[35]
	1098	↑	($P = 0.0002$)	↓	($P < 0.0001$)	Nicotinamide, phosphate	[35]
	1608	↑	($P = 0.0200$)	↓	($P = 0.0007$)	Nicotinamide	[35]
	1688	↑	($P = 0.0070$)	↓	($P = 0.0070$)	Nicotinamide	[35]
NAD^+	888	–	($P = 0.6000$)	↑	($P < 0.0001$)	Phosphate	[35]
	1035	(↓)	($P = 0.0700$)	↑	($P = 0.0100$)	Nicotinamide	[35]
	1119	↓	($P = 0.0200$)	↑	($P = 0.0010$)	Ribose, pyrophosphate	[35]
	1313	↓	($P = 0.0030$)	↑	($P < 0.0001$)	Adenine	[35]
	1333	–	($P = 0.8000$)	↑	($P < 0.0001$)	Adenine & ribose	[35]
	1580	↓	($P = 0.0002$)	↑	($P = 0.0100$)	Adenine, ribose & nicotinamide	[35]
Cytochrome c (Fe^{2+})	752	↑	($P = 0.0020$)	↓	($P < 0.0001$)	ν_{15} Pyrrole breathing	[34]
	806	–	($P = 0.6000$)	↓	($P < 0.0002$)	ν_6 Pyrrole breathing	[34]
	1127	–	($P = 0.4000$)	↓	($P = 0.0090$)	ν_{22} Assymmetric pyrrole half ring	[34]
	1505	↑	($P = 0.0060$)	↓	($P = 0.0200$)	ν_3 Spin-state	[34]
Cytochrome c (Fe^{3+})	569	–	($P = 0.4000$)	↑	($P = 0.0015$)	ν_{21} Pyrrole folding	[34]
	1582	↓	($P = 0.0006$)	↑	($P = 0.0300$)	ν_{19} Spin-state	[34]
	1638	↓	($P = 0.0470$)	↑	($P = 0.0009$)	ν_{37} Spin-state	[34]

Peaks for the targeted biomarkers were assigned as depicted in the Raman difference spectra in Figure 3b. An upward arrow (↑) indicates an increase in peak intensity, a downward arrow (↓) indicates a decrease, and a hyphen (-) indicates no change. Intensities of the individual peaks of the difference spectra were analyzed by a one-sample t-test (two-tailed, $n = 4$); the resulting P values are displayed in brackets.

stable depolarization was already observed at 52.6 ± 3.0 s in the microfluidic system (mean ± SEM; $n = 4$; unpaired t-test, two-tailed: $P = 0.0004$) (Figure 4a). As seen for the redox state, the hypoxia-induced depolarization was fully reversible upon return to normoxia (Figure 4a,c).

2.5. Visualization of Cellular Contraction via Live-Cell Imaging

PASMC depolarization is known to induce calcium (Ca^{2+}) influx, thereby initiating cellular contraction.[8] For quantification of the hypoxia-induced contraction of single cells, image series were recorded during the transition from i) normoxia to hypoxia and ii) hypoxia to recovery (Figure 4a). The resulting images were processed using image correlation[36,37] and segmentation to estimate the cellular contraction (Figure 4d; for details, see the Methods section). Representative pictures under normoxia and hypoxia are shown in Figure 4e,f. Upon hypoxic exposure, the PASMCs contracted while simultaneously showing the changes in redox state and membrane potential described in the previous sections (Figure 4a,d,g). However, in contrast to the reversibility of redox state and membrane potential, the hypoxia-induced contraction continued (albeit at a decreased rate) upon return to normoxic conditions (recovery; Figure 4a,d).

3. Discussion

The key features of acute O_2 sensing in mammalian cells include i) changes in the cellular and mitochondrial redox state, ii) the electrophysiological response (e.g., changes in membrane potential) and iii) the resulting cellular reaction (e.g., the contraction of pulmonary vascular smooth muscle cells).[10] To fully elucidate the molecular events underlying the multifactorial processes of cellular O_2 sensing, these key features should preferably be observed simultaneously in the same cells. To address this need, we have developed a multimodal and label-free technique that can be applied to a wide variety of O_2-sensitive cells.

The core of the presented technique is a sealed microfluidic system that enables multimodal recordings (Raman spectroscopy, patch-clamp electrophysiology, and live-cell imaging) under tightly controlled and continuously measured pO_2. The microfluidic system allows user-friendly replacement of the patch pipette capillary and fits onto commercially available culture dishes with a lowered glass bottom, which is economical, allows the exchange of samples with minimal effort, and enables measurement of adherent cells without the need for enzymatic or mechanical dissociation, which could negatively influence cellular viability, function or response. Commercially available imaging cell culture dishes are routinely equipped with a lowered glass bottom (compared to the cell culture dish's periphery), which is not only advantageous to enable high-quality live-cell imaging and Raman spectroscopy but is a prerequisite for fluid flow within the microfluidic system. Consequently, cell culture dishes with an entirely flat bottom would not be compatible with our microfluidic system.

Furthermore, the time span for switches between normoxic and hypoxic pO_2 can be varied by the choice of the perfusion velocity, that is, higher flow rates to achieve faster pO_2-switches

© 2021 The Authors. Small Methods published by Wiley-VCH GmbH

23669608, 2021, 10, Downloaded from https://onlinelibrary.wiley.com/doi/10.1002/smtd.202100470 by Justus-Liebig-Universitat, Wiley Online Library on [24/11/2022]. See the Terms and Conditions (https://onlinelibrary.wiley.com/terms-and-conditions) on Wiley Online Library for rules of use; OA articles are governed by the applicable Creative Commons License

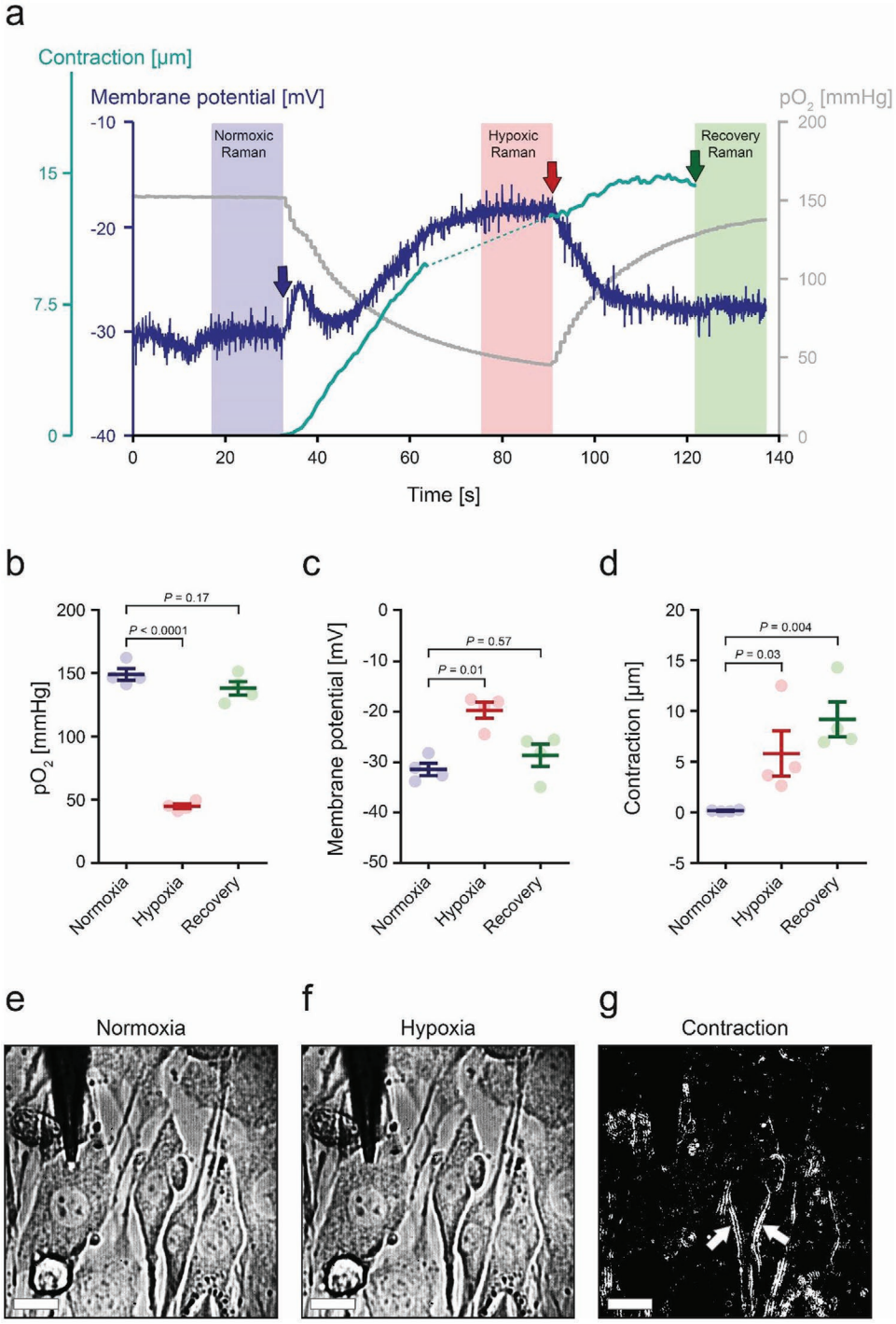

Figure 4. Validation of the setup with regard to electrophysiological and mechanical response of PASMCs to hypoxia. a) Representative traces for simultaneous recording of membrane potential (dark blue), pO_2 (grey), and PASMC contraction (turquoise). Color-coded arrows indicate time-points of data taken for statistical analysis of pO_2 (see panel (b)), membrane potential (see panel (c)), and contraction (see panel (d)). The time intervals during which Raman spectra were taken are indicated by shaded colored areas (light blue, red, and green for normoxia, hypoxia, and recovery, respectively). No images were taken during hypoxic Raman spectroscopy, hence the turquoise line is dashed for this interval. b–d) Statistical analysis of experiments depicted in panel (a). Data were analyzed by one-way ANOVA followed by Tukey's post hoc test and are shown as mean ± SEM ($n = 4$). e,f) Visualization of PASMC contraction: bright-field image of PASMCs under normoxia (e) and hypoxia (f). g) Segmented displacement magnitude for visualization of contraction. High intensities (white) indicate areas of contraction. Scale bar = 30 µm.

© 2021 The Authors. Small Methods published by Wiley-VCH GmbH

23669608, 2021, 10, Downloaded from https://onlinelibrary.wiley.com/doi/10.1002/smtd.202100470 by Justus-Liebig-Universitat, Wiley Online Library on [24/11/2022]. See the Terms and Conditions (https://onlinelibrary.wiley.com/terms-and-conditions) on Wiley Online Library for rules of use; OA articles are governed by the applicable Creative Commons License

and vice versa (see Figure S5, Supporting Information). However, high perfusion velocities could induce undesired noise in patch-clamp recordings or lead to detachment of the cell during experiments. In contrast, lower perfusion velocities would not have unwanted effects with regard to noise and cell viability but would delay the application of hypoxia. In the present study, 1.5 mL min^{-1} was found to be optimal to ensure rapid application of hypoxia with minimal noise, while maintaining the cell's viability. However, the decision on perfusion velocity can be individually taken and is determined by the specific scientific question that the user intends to answer.

Raman spectroscopy, which detects vibrational energy levels of specific molecular bonds, allowed for the simultaneous, specific, and label-free determination of cellular and mitochondrial biomarkers that are possibly involved in acute O_2 sensing in mammalian cells (i.e., cytochrome c (Fe^{2+}/Fe^{3+}) or NADH/NAD^+).[8] To enable Raman spectroscopy of these biomarkers, a laser wavelength was chosen that is in resonance with cytochrome c.[34] Further, the microfluidic system was made of a polymer with limited interference with the Raman peaks of the targeted biomarkers (Figure S2, Supporting Information). Notably, with the technique presented here, other cellular molecules or biomarkers of interest could be investigated by choosing either a distinct polymer, a distinct laser wavelength, or both. Moreover, the microfluidic system can be combined with other imaging techniques, for example, fluorescence, Ca^{2+}-imaging, or coherent techniques. Thus, our approach is applicable to most scientific questions related to redox signaling in O_2 sensing processes.

For analysis of biomarkers, Raman spectra were analyzed using linear regression of the complete difference spectral data. This approach resulted in an adequate correlation over the entire spectral area. Compared with analysis of certain Raman peak intensities only, examining the correlation of the complete spectral region is beneficial for the following reason: Many possible Raman peaks of distinct molecules overlap with those of other molecules and can thus be associated with different possible biomarkers, which could lead to faulty interpretation of the data. In our study, the linear regression model was based on reference spectra from the scientific literature, which required an adaptation of the intensities. However, direct recording of Raman spectra from the targeted biomarkers in a pure form, in different oxygenation states, and with the same setup should eliminate the need to adjust the spectra. The Raman spectroscopic results, presented in Figure 3 and Table 3, showed reversible changes in the redox state of the targeted biomarkers in response to hypoxia. The correlation implies that the linear combination, acquired by classical least square fitting, explains a significant portion of the difference spectra. However, not all information in the difference spectra can be explained by NADH/NAD^+ and cytochrome c (Fe^{2+}/Fe^{3+}). Therefore, adding ancillary biomolecules involved in cellular O_2 sensing and signaling processes (e.g., ubiquinone,[38,39] calmodulin,[40] or phospholipids;[41] Figure S6, Supporting Information) to the linear regression may be advantageous. In larger studies, multivariate analysis (e.g., principal component analysis or linear discriminant analysis) could be used to classify the data further and to gain insights into differences in the resulting spectra. However, these data-driven methods would not enable direct assessment of the contributions of selected biomolecules.

In patch-clamp measurements, the observed hypoxia-induced membrane depolarization is in accordance with well-recognized findings from several laboratories reporting a hypoxia-induced inhibition of voltage-gated K^+ channels.[8,31,42–44] The resulting increase in membrane potential is crucial for the initiation of hypoxic pulmonary vasoconstriction or systemic vasodilation. Here, we performed whole-cell current-clamp recordings to determine membrane potential. However, patch-clamp measurements could similarly be performed in voltage-clamp mode to measure ionic currents involved in O_2 sensing processes. Moreover, due to the versatile patch pipette, all conventional patch-clamp configurations for single-channel recordings (cell-attached, inside out, or outside out) are applicable in the presented setup.

Consistent with the observed change in redox state and membrane depolarization, we observed hypoxia-induced contraction of PASMCs by implementing simultaneous live-cell imaging during the transitions between normoxia and hypoxia. Although the ongoing contraction upon return to normoxia (recovery), as observed by live-cell imaging, is in contrast to the fully reversible membrane potential as well as the behavior of the cellular and mitochondrial biomarkers, it highlights the possibility of correlating the ongoing cellular processes in a time-resolved manner. Furthermore, it might reveal a currently unknown coupling of events, which requires further investigation.

4. Conclusion

Although our multimodal setup has here been used to measure PASMCs, it is applicable and transferrable to any other cell type. Consequently, this technique may enable new measurement opportunities in a wide variety of scientific applications. The results presented here conclusively demonstrate that our multimodal approach allows—for the first time—simultaneous measurement of the cellular processes involved in O_2 sensing. Thus, our technique has the unique ability to provide an unambiguous picture of the key cellular events underlying all mammalian O_2 sensing processes. Moreover, our technique has the potential to allow direct observation of the upstream or downstream effects of pharmacological or genetic interventions that target these key events.

5. Experimental Section

Cell Isolation and Sample Preparation: The isolation of murine PASMCs from C57BL/6J mice was approved by the "Institutional Animal Investigation Care and Use Committee" and the appropriate governmental committee (AZ G70/2019). Seven to 10 days prior to experiments, PASMCs from three male mice at the age of 12–16 weeks were isolated as previously described[45,46] and grown on glass bottom dishes (35/10 mm, Greiner Bio-One, Frickenhausen, Germany). Note, that approximately 60–70% of the cell culture dish´s growth area (glass bottom) should be covered with cells (i.e., a confluency of 60–70%). Although a confluency of less than 60% does not necessarily prohibit successful experiments, it might lower the chance of cells being present in the measurement section.

Design and Manufacturing of the Microfluidic System: The microfluidic system was designed in 3D CAD software (Siemens NX, Siemens AG, Munich, Germany) to fit onto a commercial cell culture dish with a lowered glass bottom (35/10 mm, Greiner Bio-One) that was suitable for both imaging and Raman spectroscopy. For insertion of all components

© 2021 The Authors. Small Methods published by Wiley-VCH GmbH

23669608, 2021, 10, Downloaded from https://onlinelibrary.wiley.com/doi/10.1002/smtd.202100470 by Justus-Liebig-Universitat, Wiley Online Library on [24/11/2022]. See the Terms and Conditions (https://onlinelibrary.wiley.com/terms-and-conditions) on Wiley Online Library for rules of use; OA articles are governed by the applicable Creative Commons License

(i.e., electrodes and perfusion tubes) and to promote optimal fluid flow inside the microfluidic system, the pipes within the microfluidic system were arranged at specific angles ($\measuredangle$): 60° for the inlet, 55° for the outlet, and 45° for the patch pipette, oxygen sensor, and reference electrode (Table 2 and Figure S1, Supporting Information). To make the design as compact as possible, the ends of the pipes for the reference electrode and the O_2 sensor were merged into the outlet and inlet pipe, respectively (Figure 1c). The pipes of the inlet and the O_2 sensor were equipped with a thread hole for insertion of PEEK one-piece fingertight fittings and their corresponding ferrules (Scantec, Mölndal, Sweden). During mounting of the components, that is, tightening of the PEEK-fittings, the ferrule was crimped onto the O_2-sensor and inlet tube, respectively, and ensured the gas- and fluid impermeability of these pipes. In addition, the pipes for the outlet tube, the rubber insulation for the patch pipette, and the reference electrode were designed to be tight-fit to their respective components. The geometry chosen for the pipes in combination with the fittings and ferrules ensured a tight seal between the distinct components and the microfluidic system, thus reliably preventing air or fluid leakage through undesired gaps.

After design, the microfluidic system was milled in polymethylpentene using a computer numerical control machine (Friedrich Deckel AG, FP5NC, Munich, Germany). All edges of the microfluidic system were cut to 45° and excess material was removed (Figure 1a,c).

Fluid Simulations of the Microfluidic System: The fluid flow through the microfluidic system was too complex to be solved analytically and was therefore simulated with computational fluid dynamics using the commercial software Ansys CFX 16 (ANSYS, Inc., Canonsburg, Pennsylvania, USA). Different microfluidic cell geometries with varying configurations of pipes for the inlet, outlet, and patch pipette were created and discretized into tetrahedral grids with 120k–150k nodes, and flow properties were solved in each computational node in the grids. Ansys CFX uses an element-based finite volume method to discretize the equations of fluid motion[47] and here a second-order accurate advection scheme was used for the momentum and continuity equations and a second-order backward Euler scheme for transient terms. The transient solver for laminar flow was used with a convergence criterion of root mean square residuals below 10^{-6} and the transient time step was chosen as 0.01 s with a total simulation time of 200 s. The inlet boundary condition was approximated as a constant velocity in the normal direction of the inlet, the outlet boundary was set as an average static pressure of –0.2 bar and all walls were given a no-slip boundary condition. A volume of fluids model was implemented to account for both the gas and liquid phase.[48] The fluids in the simulation were defined as water at 37 °C and air at 25 °C, and the flow rate in the simulations was perpetually set to 5 mL min^{-1}. The time-dependent simulations were then performed to investigate the rise of fluid levels into the measurement section as well as the flow field in the cell chamber.

Patch-Clamp Electrophysiology: Fire-polished patch pipettes with a tip resistance of 3–5 MΩ were pulled from borosilicate glass capillaries (Sutter instruments, Novato, California, USA) using a DMZ universal electrode puller (Zeitz, Martinsried, Germany). Afterwards they were filled with an intracellular analogous solution containing 105 mM K^+-aspartate, 25 mM KCl, 4 mM NaCl, 1 mM $MgCl_2$, 4 mM Mg-ATP, 10 mM EGTA, and 10 mM HEPES (pH adjusted to 7.2 with 1 M KOH). Liquid junction potential (+12.3 mV) was corrected electronically and cellular membrane potential was recorded in current-clamp mode (I = 0, whole-cell configuration). Data were filtered at 2.9 kHz and sampled at 50 Hz using an EPC10 USB single amplifier (HEKA, Lambrecht, Germany) controlled by Patchmaster software (HEKA).

During patch-clamp recordings, PASMCs (grown in passage 0) were continuously perfused with extracellular analogous bath solution (Tyrode's solution: 126.7 mM NaCl, 5.4 mM KCl, 1.8 mM $CaCl_2$, 1.05 mM $MgCl_2$, 0.42 mM NaH_2PO_4, 22 mM $NaHCO_3$, and 10 mM Glucose, pH 7.4) at a continuous flow rate of 1.5 mL min^{-1}. The Tyrode's solution was pre-heated to 37 °C using an in-line solution heater (SHM-8, Warner Instruments, Hamden, USA) and gassed with either a normoxic (21% O_2 ($\triangleq$ 159.7 mmHg), 5.3% CO_2 ($\triangleq$ 40.3 mmHg), rest N_2) or a hypoxic (1% O_2 ($\triangleq$ 7.6 mmHg), 5.3% CO_2, rest N_2) gas mixture. The solution was delivered to the microfluidic system via a gravity-driven and valve-controlled perfusion system (VC3-8xG, Ala Scientific Instruments, Farmingdale, New York, USA). An optical O_2 sensor (Bare Fiber Minisensor OXB430, Firesting O_2, PyroScience, Aachen, Germany) which was connected to an analog-digital channel of the patch-clamp amplifier continuously logged the pO_2 inside the microfluidic system. The pO_2 trace was time-corrected by 3.3 s, since the default response time of the O_2 sensor in liquids was 3.3 ± 0.5 s (mean ± SEM, n = 6). For patch-clamp recordings, the patch pipette was inserted into the microfluidic system via an electronically driven micromanipulator (MP-225, Sutter Instruments). After insertion of the patch pipette, the channel was sealed with a thin-walled rubber insulation. The insulation enabled a flexible and precise 3D-movement of the patch pipette, which was only limited by the boundaries of the microfluidics' pipe. Analysis was performed with Fitmaster software (HEKA), Igor Pro 7 (Wavemetrics, Lake Oswego, Oregon, USA), and Prism (GraphPad Software, San Diego, California, USA).

Image Acquisition and Processing for Estimation of Cellular Contraction: For image acquisition, the microfluidic system was illuminated with a red LED (LED635, Thorlabs, Newton, New Jersey, USA) that was mounted above the microfluidic system (Figure 2a). Image acquisition was initiated simultaneously with the switch from normoxia to hypoxia and the switch from hypoxia to recovery (Figure 2c). Time series of 50 consecutive images were acquired with a frame rate of 1.5 images s^{-1} using a complementary metal-oxide semiconductor (CMOS) camera (Mako U-503B, Allied Vision, Thuringia, Germany) with a resolution of 2592 × 1944 pixels and a pixel size of 2.2 µm.

A schematic workflow of the image processing is outlined in Figure S7, Supporting Information. First, image correlation was used to estimate the hypoxia-induced contraction of the PASMCs by applying an in-house C-code initially created for speckle correlation.[49] For calculations, the first image of each experiment served as the reference frame. The total 2592 × 1944 pixels per image were divided into image patches of 256 × 256 pixels, each separated by 32 pixels. This resulted in a resolution of 81 × 60 patches per image. To determine specifically the motions associated with cellular contraction, the patch pipette and detached cells were masked by manually applying operators of mathematical morphology using the functions imdilate and imerode in MATLAB R2019a (MathWorks, Massachusetts, USA) with circular structuring elements. Finally, using the MATLAB function graythresh,[50] a constriction threshold was computed to separate and exclude those pixels that exhibited negligible motion from those of the silhouette of the PASMC (Figure S7, Supporting Information). This procedure separated the cellular contraction from background movements. An average PASMC contraction was then estimated for each consecutive frame (Figure 4a,d,g). To show the contraction of the PASMCs with adequate resolution, the MATLAB function OpticalFlowFarneback was used and the intensities were enhanced with histeq as seen in Figure 4g and Figure S7, Supporting Information. These functions allowed the full image resolution to be retained in order to show clearly the outline of the PASMCs, but the precision did not match that of the actual image correlation.

Raman Acquisition and Processing: For Raman acquisition, a Shamrock 303i spectrometer (Andor Technology, Belfast, UK) equipped with a 532 nm diode-pumped solid-state (DPSS) laser (Altechna, Vilnius, Lithuania) was connected to the microscope objective. Raman spectra were recorded with an integration time of 3 × 5 s and a laser power of 34 mW measured after the neutral density filter.

To remove all static information in the acquired spectra (i.e., fluorescent background and molecular vibrations that were not affected by changes in O_2 levels), difference spectra (hypoxia – normoxia and recovery – hypoxia, respectively) were calculated with MATLAB R2019a (MathWorks) and used for further analysis. This approach specifically separated the O_2-sensitive molecular vibrations from the entire Raman spectra. Note that the standard deviation of the measurement noise will increase as $\sigma' = \sqrt{\sigma_1^2 + \sigma_2^2}$ (assuming Gaussian-distributed noise), where $\sigma_{1,2}$ and σ' are the noise standard deviations of the initial and resulting signals respectively.[51] To circumvent noise accumulation, the data were upsampled by acquiring three measurements per O_2 level (normoxia, hypoxia, and recovery). Three measurements for the three different O_2 levels yield 3 × 3 = 9 difference spectra for both the transition from normoxia to hypoxia and from hypoxia to recovery. For four distinct experiments, the sample size becomes 4 × 3 × 3 = 36 difference spectra.

© 2021 The Authors. Small Methods published by Wiley-VCH GmbH

23669608, 2021, 10, Downloaded from https://onlinelibrary.wiley.com/doi/10.1002/smtd.202100470 by Justus-Liebig-Universitat, Wiley Online Library on [24/11/2022]. See the Terms and Conditions (https://onlinelibrary.wiley.com/terms-and-conditions) on Wiley Online Library for rules of use; OA articles are governed by the applicable Creative Commons License

The difference spectra were processed through an in-house-developed Monte Carlo Savitzky–Golay filter, which was designed to reduce subjective influences in choices of filter parameters and optimize the result to resemble a biomarker signature (see the paragraph on MATLAB implementation at the end of this section). A conventional Savitzky–Golay filter applies input variables for polynomial order and segment length. The filter proceeds to iterate over the signal and replaces the observed signal with a reconstruction based on values from local optimally fitted polynomials.[52] A dictionary of Chebyshev polynomials as basis vectors for the fitting was utilized. An objective choice of filter parameters was achieved by randomizing in a Monte Carlo fashion, using a maximum polynomial order of five and a segment length of up to 15 pixels. For a random set of filter parameters, the signal was filtered and then added to a weighted sum until the signal had converged. The weighting was done by correlation with a random linear combination of spectra from known biomarkers (cytochrome c (Fe^{2+}/Fe^{3+}) and NADH/NAD^+, see next paragraph) which yields the correlation coefficient,

$$r = \frac{\sum_i \Delta S(i)\Theta(i)}{\left(\sum_i \Delta S(i)^2\right)\left(\sum_i \Theta(i)^2\right)} \tag{3}$$

where ΔS is the processed difference spectrum and Θ is the randomized linear combination of biomarkers. For each iteration, the filtered signal (ΔS) was then multiplied by $|r|^2$, before addition to the cumulative sum of results. After iterating over many random filter parameters, the signal converged to a processed signal that was optimized to resemble an unknown linear combination of a set of biomarkers. A schematic of the whole Raman analysis, including the filtering, is shown in Figure 3a – the remaining steps of the scheme are explained in the following section.

Raman Spectra Reconstruction of the Biomarkers NADH and Cytochrome c: The Raman signal from a PASMC was the linear combination of the Raman spectra of all molecular bonds of the cell that were affected by the emitted laser line. The spectral changes due to the molecular vibrations of cytochrome c (Fe^{2+}/Fe^{3+}) and NADH/NAD^+ can be estimated as a linear combination of their respective spectra. The spectra were derived from the work of Hu et al.[34] and Yue et al.,[35] by fitting Lorentz peaks to their results,

$$L = \sum_i \frac{A_i}{\left((x-a_i)^2 - b_i^2\right)^2} \tag{4}$$

where A_i, a_i, and b_i are the amplitude, position,, and width of the i:th peak, respectively. The reconstructions were made in the range 550–1700 cm^{-1}, to overlap with the spectral region of the experiments.

Linear Regression of Adjusted Biomarker Raman Spectra: By least-squares fitting, the processed difference spectrum can be decomposed into components that can be associated with the respective biomarker spectra. The NADH/NAD^+ and cytochrome c spectra were reconstructed from measurements performed with an excitation wavelength of 515[34] and 413 nm,[35] respectively. A consequence of the excitation wavelengths being different from that of the experimental setup (532 nm) was that the peak intensities were likely to be different. Therefore, the peak intensities A_i were adjusted to improve the fitting of the processed difference spectra to highlight the changes. The adjustment was done by minimizing the cost function,

$$f(\boldsymbol{A}) = \max\{|(S(\boldsymbol{A})\left(S(\boldsymbol{A})^T S(\boldsymbol{A})\right)^{-1} S(\boldsymbol{A})^T - 1)\Delta S_i|^2\}, i = 1,2 \tag{5}$$

where $S(\boldsymbol{A})$ is a matrix containing biomarker spectra, $\boldsymbol{A}$ is an array with all the intensities for the individual Lorentz peaks (Equation (4)) in each spectrum, and $\Delta S_{1,2}$ is the processed difference spectrum for the two consecutive transitions—normoxia to hypoxia and hypoxia to recovery. The optimization was done with the simplex search method.[53] The initial biomarker spectra and their adjusted counterparts are shown in Figure S8, Supporting Information.

MATLAB Implementation of the Monte Carlo Savitzky–Golay Filter: This section contains two MATLAB functions, implemented in MATLAB R2019a (MathWorks). The first function was the Monte Carlo Savitzky–Golay filter used in this work to process difference spectra acquired from Raman measurements. The second function was used by the main function to generate the Chebyshev dictionary used as a basis in the Savitzky–Golay filter.

Matlab Function 1: function [mu, sigma] = f(data,ref,order,segment, maxiter)

%Output mean signal, mu, and standard deviation, sigma. Indata is the unprocessed data, x, and a reference signal that is assumed to exist in unfiltered data. Savitzky–Golay coefficients are chosen randomly in the range given by order and segment ([min_value, max_value]). The number of iterations is set by maxiter.

```
mu = zeros(size(data,1),1);
variance = zeros(size(data,1),1);
for i = 1 : maxiter
%randomize filter parameters
polyorder = min(order) + randi(diff(order) + 1)–1;
polysegment = min(segment) + randi(diff(segment) + 1)–1;
%chebyshev polynomial basis vectors
y = linspace(–1, 1, polysegment);
x = linspace(–1, 1, size(data,2));
C = Cheby2D(x, y, polyorder);
D = reshape(C, [size(C,1) * size(C,2), size(C,3)]);
%Savitzky–Golay filter
T = padarray(data(:,randperm(size(data,2))), [polysegment,...0],"replicate");
r = zeros(size(T,1), 1);
id = polysegment+round(0.5*polysegment);
for j = 1 : size(data, 1) + polysegment + 1
t = T(j : j + polysegment–1,:);
t = t(:);
patch = D * (D \ t);
r(j) = patch(id);
end
r = r(polysegment + 1 : end–polysegment);
%Correlation with random linear combination of ref
a = 2*rand(size(ref,2), 1)–1;
c = corr(r, normc(ref * a));¨
%Calculating weighted average and variance
mu = mu + (ref * abs(c));
variance = variance + (abs(c) * r).^2;
end
mu = mu/maxiter;
variance = variance/maxiter–mu.^2;
sigma = sqrt(variance);
end
```

Matlab Function 2: function Z = Cheby2D(x,y,n)

%Chebyshev polynomial basis vectors in space defined by x and y, up to order, n.

```
[X,Y] = meshgrid(x(:),y(:));
[N,M] = size(X);
Zx = ones(N,M,n+1);
Zy = Zx;
Zx(:,:,2) = X;
Zy(:,:,2) = Y;
for i = 3 : n+1
Zx(:,:,i) = 2*X.*Zx(:,:,i–1) + Zx(:,:,i–2);
Zy(:,:,i) = 2*Y.*Zy(:,:,i–1) + Zy(:,:,i–2);
End
index = [nchoosek(0:n,2);nchoosek(n: –1:0,2)];
index(sum(index,2)>n,:) = [];
index = index + 1;
Z = ones(N,M,1+size(index,1));
for i = 2 : size(index,1) + 1
Z(:,:,i) = Zx(:,:,index(i–1,1)).*Zy(:,:,index(i–1,2));
End
end
```


© 2021 The Authors. Small Methods published by Wiley-VCH GmbH

23669608, 2021, 10, Downloaded from https://onlinelibrary.wiley.com/doi/10.1002/smtd.202100470 by Justus-Liebig-Universitat, Wiley Online Library on [24/11/2022]. See the Terms and Conditions (https://onlinelibrary.wiley.com/terms-and-conditions) on Wiley Online Library for rules of use; OA articles are governed by the applicable Creative Commons License

Supporting Information

Supporting Information is available from the Wiley Online Library or from the author.

Acknowledgements

The author would like to acknowledge Carmen Homberger, Susanne Lich, and Karin Quanz for technical assistance as well as Martin Lund and Fredrik Nilsson from the Central Workshop, Luleå University of Technology. This study was supported by the Deutsche Forschungsgemeinschaft (DFG, German Research Foundation) – Project numbers 452531259 and 268555672 – CRC 1213, project A06, and the Swedish Research Council (grant 2016–04220). Portions of the licentiate thesis of Joel Wahl (i.e., Figure 1c,d) are incorporated into this report. Editorial support at the final draft stage was provided by Claire Mulligan, Ph.D. (Beacon Medical Communications Ltd, Brighton, UK) and funded by the University of Giessen.

Open access funding enabled and organized by Projekt DEAL.

Conflict of Interest

The authors declare no conflict of interest.

Data Availability Statement

The data that support the findings of this study are available from the corresponding authors upon reasonable request.

Keywords

acute oxygen sensing, hypoxia, live-cell imaging, microfluidics, patch clamps, Raman spectroscopy, redox reactions, simultaneous assessment of cellular responses

Received: April 30, 2021
Revised: July 23, 2021
Published online: August 21, 2021

[1] B. L. Krock, N. Skuli, M. C. Simon, *Genes Cancer* **2011**, *2*, 1117.
[2] V. H. Haase, *Am J. Physiol.: Ren. Physiol.* **2010**, *299*, F1.
[3] J. López-Barneo, R. del Toro, K. L. Levitsky, M. D. Chiara, P. Ortega-Sáenz, *J. Appl. Physiol.* **2004**, *96*, 1187.
[4] L. Gao, P. González-Rodríguez, P. Ortega-Sáenz, J. López-Barneo, *Redox Biol.* **2017**, *12*, 908.
[5] World Health Organization, *Global health estimates: Leading causes of death. 2020*, https://www.who.int/data/gho/data/themes/mortality-and-global-health-estimates/ghe-leading-causes-of-death (accessed: April 2021).
[6] G. L. Semenza, *N. Engl. J. Med.* **2011**, *365*, 537.
[7] J. López-Barneo, R. Pardal, P. Ortega-Sáenz, *Annu. Rev. Physiol.* **2001**, *63*, 259.
[8] N. Sommer, N. Alebrahimdehkordi, O. Pak, F. Knoepp, I. Strielkov, S. Scheibe, E. Dufour, A. Andjelković, A. Sydykov, A. Saraji, A. Petrovic, K. Quanz, M. Hecker, M. Kumar, J. Wahl, S. Kraut, W. Seeger, R. T. Schermuly, H. A. Ghofrani, K. Ramser, T. Braun, H. T. Jacobs, N. Weissmann, M. Szibor, *Sci. Adv.* **2020**, *6*, eaba0694.
[9] A. Moreno-Domínguez, P. Ortega-Sáenz, L. Gao, O. Colinas, P. García-Flores, V. Bonilla-Henao, J. Aragonés, M. Hüttemann, L. I. Grossman, N. Weissmann, N. Sommer, J. López-Barneo, *Sci. Signaling* **2020**, *13*, eaay9452.
[10] E. D. Michelakis, I. Rebeyka, X. Wu, A. Nsair, B. Thébaud, K. Hashimoto, J. R. B. Dyck, A. Haromy, G. Harry, A. Barr, S. L. Archer, *Circ. Res.* **2002**, *91*, 478.
[11] A. N. Vjotosh, *Biochemistry* **2020**, *85*, 40.
[12] P. Lee, N. S. Chandel, M. C. Simon, *Nat. Rev. Mol. Cell Biol.* **2020**, *21*, 268.
[13] M. Schwarzländer, T. P. Dick, A. J. Meyer, B. Morgan, *Antioxid. Redox Signaling* **2016**, *24*, 680.
[14] T. S. Blacker, M. R. Duchen, *Free Radical Biol. Med.* **2016**, *100*, 53.
[15] C. T. Dooley, T. M. Dore, G. T. Hanson, W. C. Jackson, S. J. Remington, R. Y. Tsien, *J. Biol. Chem.* **2004**, *279*, 22284.
[16] A. Wiederkehr, N. Demaurex, *Nat. Methods* **2017**, *14*, 671.
[17] N. Sommer, O. Pak, S. Schörner, T. Derfuss, A. Krug, E. Gnaiger, H. A. Ghofrani, R. T. Schermuly, C. Huckstorf, W. Seeger, F. Grimminger, N. Weissmann, *Eur. Respir. J.* **2010**, *36*, 1056.
[18] U. Topf, I. Suppanz, L. Samluk, L. Wrobel, A. Böser, P. Sakowska, B. Knapp, M. K. Pietrzyk, A. Chacinska, B. Warscheid, *Nat. Commun.* **2018**, *9*, 324.
[19] J. N. Cobley, H. Husi, *Antioxidants* **2020**, *9*, 315.
[20] P. Zhu, T. Oe, I. A. Blair, *Rapid Commun. Mass Spectrom.* **2008**, *22*, 432.
[21] D. P. Jones, Y.-M. Go, *Diabetes, Obes. Metab.* **2010**, *12*, 116.
[22] J. Birk, T. Ramming, A. Odermatt, C. Appenzeller-Herzog, *Front. Genet.* **2013**, *4*, 108.
[23] L. Shi, X. Liu, L. Shi, H. T. Stinson, J. Rowlette, L. J. Kahl, C. R. Evans, C. Zheng, L. E. P. Dietrich, W. Min, *Nat. Methods* **2020**, *17*, 844.
[24] H. J. Butler, L. Ashton, B. Bird, G. Cinque, K. Curtis, J. Dorney, K. Esmonde-White, N. J. Fullwood, B. Gardner, P. L. Martin-Hirsch, M. J. Walsh, M. R. McAinsh, N. Stone, F. L. Martin, *Nat. Protoc.* **2016**, *11*, 664.
[25] U. Neugebauer, S. H. Heinemann, M. Schmitt, J. Popp, *Anal. Chem.* **2011**, *83*, 344.
[26] F. Knoepp, J. Wahl, A. Andersson, J. Borg, N. Weissmann, K. Ramser, *Sensors* **2018**, *18*, 3238.
[27] B. Sakmann, E. Neher, *Annu. Rev. Physiol.* **1984**, *46*, 455.
[28] L. D. Plant, D. Xiong, J. Romero, H. Dai, S. A. N. Goldstein, *Cell Rep.* **2020**, *30*, 2225.
[29] A. Alrifaiy, J. Borg, O. A. Lindahl, K. Ramser, *Biomed. Eng. Online* **2015**, *14*, 36.
[30] J. H. Ferziger, M. Peric, R. L. Street, in *Computational Methods for Fluid Dynamics*, 4th ed., Springer, New York **2020**.
[31] N. Sommer, M. Hüttemann, O. Pak, S. Scheibe, F. Knoepp, C. Sinkler, M. Malczyk, M. Gierhardt, A. Esfandiary, S. Kraut, F. Jonas, C. Veith, S. Aras, A. Sydykov, N. Alebrahimdehkordi, K. Giehl, M. Hecker, R. P. Brandes, W. Seeger, F. Grimminger, H. A. Ghofrani, R. T. Schermuly, L. I. Grossman, N. Weissmann, *Circ. Res.* **2017**, *121*, 424.
[32] N. A. Brazhe, M. Treiman, B. Faricelli, J. H. Vestergaard, O. Sosnovtseva, *PLoS One* **2013**, *8*, e70488.
[33] N. A. Brazhe, M. Treiman, A. R. Brazhe, N. L. Find, G. V. Maksimov, O. V. Sosnovtseva, *PLoS One* **2012**, *7*, e41990.
[34] S. Hu, I. K. Morris, J. P. Singh, K. M. Smith, T. G. Spiro, *J. Am. Chem. Soc.* **1993**, *115*, 12446.
[35] K. T. Yue, C. L. Martin, D. Chen, P. Nelson, D. L. Sloan, R. Callender, *Biochemistry* **1986**, *25*, 4941.
[36] P. Anuta, *IEEE Trans. Geosci. Electron.* **1970**, *8*, 353.
[37] T. J. Keating, P. R. Wolf, F. L. Scarpace, *Photogramm. Eng. Remote Sens.* **1975**, *41*, 993.

© 2021 The Authors. Small Methods published by Wiley-VCH GmbH

23669608, 2021, 10, Downloaded from https://onlinelibrary.wiley.com/doi/10.1002/smtd.202100470 by Justus-Liebig-Universitat, Wiley Online Library on [24/11/2022]. See the Terms and Conditions (https://onlinelibrary.wiley.com/terms-and-conditions) on Wiley Online Library for rules of use; OA articles are governed by the applicable Creative Commons License

[38] G. Balakrishnan, P. Mohandas, S. Umpathy, *Spectrochim. Acta, Part A* **1997**, *53*, 1553.
[39] A. W. Parker, R. E. Hester, D. Phillips, S. Umapathy, *J. Chem. Soc., Faraday Trans.* **1992**, *88*, 2649.
[40] B. A. Seaton, J. F. Head, R. C. Lord, G. A. Petsko, *Biochemistry* **1983**, *22*, 973.
[41] K. Czamara, K. Majzner, M. Z. Pacia, K. Kochan, A. Kaczor, M. Baranska, *J. Raman Spectrosc.* **2015**, *46*, 4.
[42] J. T. Sylvester, L. A. Shimoda, P. I. Aaronson, J. P. T. Ward, *Physiol. Rev.* **2012**, *92*, 367.
[43] S. L. Archer, B. London, V. Hampl, X. Wu, A. Nsair, L. Puttagunta, K. Hashimoto, R. E. Waite, E. D. Michelakis, *FASEB J.* **2014**, *15*, 1801.
[44] X.-J. Yuan, *Circ. Res.* **1995**, *77*, 370.
[45] G. B. Waypa, J. D. Marks, M. M. Mack, C. Boriboun, P. T. Mungai, P. T. Schumacker, *Circ. Res.* **2002**, *91*, 719.
[46] N. Weissmann, A. Dietrich, B. Fuchs, H. Kalwa, M. Ay, R. Dumitrascu, A. Olschewski, U. Storch, M. Mederosy Schnitzler, H. A. Ghofrani, R. T. Schermuly, O. Pinkenburg, W. Seeger, F. Grimminger, T. Gudermann, *Proc. Natl. Acad. Sci. USA* **2006**, *103*, 19093.
[47] *ANSYS Inc. Theory Guide*, Ansys CFX 16 Documentation, Canonsburg, Pennsylvania, USA **2014**.
[48] C. Hirt, B. Nichols, *J. Comput. Phys.* **1981**, *39*, 201.
[49] M. Sjödahl, *Appl. Opt.* **1994**, *33*, 6667.
[50] N. Otsu, *IEEE Trans. Syst. Man Cybern.* **1979**, *9*, 62.
[51] D. S. Lemons, *An introduction to stochastic processes in physics*, Johns Hopkins Univ. Press, Baltimore, USA **2002**.
[52] A. Savitzky, M. J. E. Golay, *Anal. Chem.* **1964**, *36*, 1627.
[53] J. C. Lagarias, J. A. Reeds, M. H. Wright, P. E. Wright, *SIAM J. Optim.* **1998**, *9*, 112.

© 2021 The Authors. Small Methods published by Wiley-VCH GmbH

23669608, 2021, 10, Downloaded from https://onlinelibrary.wiley.com/doi/10.1002/smtd.202100470 by Justus-Liebig-Universitat, Wiley Online Library on [24/11/2022]. See the Terms and Conditions (https://onlinelibrary.wiley.com/terms-and-conditions) on Wiley Online Library for rules of use; OA articles are governed by the applicable Creative Commons License